Journal of Colloid and Interface Science 699 (2025) 138249

Contents lists available at ScienceDirect

Journal of Colloid And Interface Science

journal homepage: www.elsevier.com/locate/jcis

Natural superoxide dismutase inspired Heterostructural N, S-Codoped $CoFe_2O_4$/MoC Electrocatalyst for highly efficient water splitting

Changcheng Lin [a], Huaibao Tang [b,***], Jun Xu [c], Dongmeng Chen [d], Xueqin Zuo [b], Qun Yang [b], Zhong Jin [g,*], Haifeng Xu [f,***], Guang Li [a,e,**]

[a] School of Materials Science and Engineering, Anhui University, Hefei 230601, PR China
[b] School of Physics and Optoelectrics, Anhui University, Hefei 230601, PR China
[c] ABA Chemicals (Shanghai) Limited, Shanghai 200063, China
[d] College of Science, China University of Petroleum, Qingdao 266580, China
[e] Anhui Key Laboratory of Information Materials and Devices, Anhui University, Hefei 230601, PR China
[f] School of Information Engineering, Suzhou University, Suzhou 234000, PR China
[g] State Key Laboratory of Coordination Chemistry, MOE Key Laboratory of Mesoscopic Chemistry, MOE Key Laboratory of High Performance Polymer Materials and Technology, Jiangsu Key Laboratory of Advanced Organic Materials, Suzhou Key Laboratory of Green Intelligent Manufacturing of New Energy Materials and Devices, Tianchang New Materials and Energy Technology Research Center, Institute of Green Chemistry and Engineering, School of Chemistry and Chemical Engineering, Nanjing University, Nanjing, Jiangsu 210023, PR China

GRAPHICAL ABSTRACT

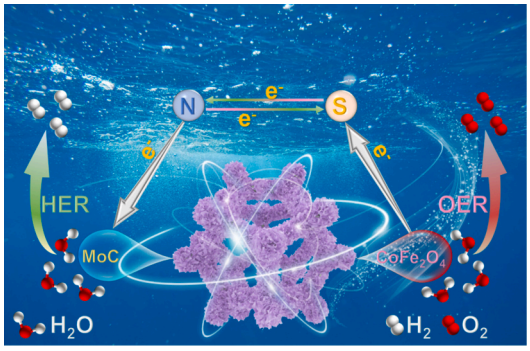

ARTICLE INFO

Keywords:
Heterostructures
Doped elements
Electron-dragging
Electrocatalytic redox reactions
N, S-$CoFe_2O_4$/MoC-NS

ABSTRACT

Current research on heterojunctions as catalysts for the oxygen evolution reaction (OER) and hydrogen evolution reaction (HER) primarily emphasizes the electron transfer processes at the heterojunction interface. However, the regulatory role of doped elements within heterostructures remains inadequately explored, despite its significant scientific implications for the advancement of efficient catalysts. Inspired by the catalytic superoxide dismutation reaction of superoxide dismutase (SOD) observed in nature, this study presents a novel heterostructural N and S co-doped $CoFe_2O_4$/MoC electrocatalyst. The incorporation of N and S induces a distinctive

* Corresponding author.
** Corresponding author at: School of Materials Science and Engineering, Anhui University, Hefei 230601, PR China.
*** Corresponding authors.
E-mail addresses: hbtang@ahu.edu.cn (H. Tang), zhongjin@nju.edu.cn (Z. Jin), xuhaifeng@ahszu.edu.cn (H. Xu), liguang1971@ahu.edu.cn (G. Li).

https://doi.org/10.1016/j.jcis.2025.138249
Received 12 March 2025; Received in revised form 11 June 2025; Accepted 19 June 2025
Available online 20 June 2025

'electron-dragging' effect within the $CoFe_2O_4$/MoC heterostructural system, selectively modulating the reception and release of electrons during HER and OER processes, thereby ensuring an optimal electron density at various active sites. The designed N, S-$CoFe_2O_4$/MoC-NS electrocatalyst achieves a total hydrolysis current density of 100 mA cm^{-2} at a potential as low as 1.47 V and maintains stable output for 300 h without degradation. Theoretical calculations and in-situ Raman spectroscopy suggest that the formation of the heterostructure and the 'electron-dragging 'effect are crucial in regulating different active sites, providing new insights into the balance between catalyst activity and stability.

1. Introduction

In water electrolysis systems, external current is utilized to overcome the energy barriers associated with the hydrogen evolution and oxygen evolution reactions (237 kJ mol^{-1}). However, the current energy conversion efficiency remains limited to 56–73 %. This level of efficiency significantly constrains the large-scale application of water electrolysis technology. As a fundamental component of this technology, electrocatalysts play a crucial role in enhancing efficiency, reducing energy consumption, and enabling low-voltage initiation. Moreover, they are essential for ensuring the selectivity, stability, and durability of the reactions [1,2]. Currently, dominant catalysts primarily rely on precious metals such as Pt, Ru, and Ir. However, the limited availability of these metals, along with the environmental pollution resulting from their extraction, highlights the urgent necessity to develop advanced non-precious metal catalysts. This development is crucial for enabling the widespread application and sustainable advancement of water electrolysis technology [3,4].

In recent years, the development of various catalysts has demonstrated remarkable performance in water splitting. Among these, heterojunction catalysts exhibit significant potential for application due to their ability to integrate the advantages of diverse materials and form complex structures, resulting in enhanced stability, selectivity, and cost-effective water electrolysis [5–7]. Current research on heterostructural electrocatalysts primarily emphasizes electron transfer at the heterojunction interface. This focus is largely attributed to the rebalancing of the Fermi level or work function induced by heterojunction coupling, which aligns with the Anderson or Mott-Schottky models [8,9]. Consequently, the distinctive properties of heterostructures primarily arise from the interactions at the heterojunction interface. These interactions include accelerated charge transfer, modulation of the electronic structure of active sites, and enhanced stability [10]. For example, Yuan et al. constructed a β-Mo_2C and α-MoC heterostructure, revealing that the strain induced by lattice mismatch enhanced the surface energy, and their synergistic effect further facilitated water splitting [11]. Similarly, Yu et al. developed a theoretical model of the Fe—$Co_{0.85}Se$/FeCo LDH system, demonstrating electron transfer from FeCo LDH to Fe—$Co_{0.85}Se$, and confirmed the bonding between Fe and Se/O through X-ray photoelectron spectroscopy (XPS) and theoretical calculations, thereby establishing an "electron transfer bridge" [12]. However, while these studies have primarily concentrated on electron transfer at heterojunction interfaces, the regulatory role of various doped elements in the electrocatalytic process has not yet been adequately addressed.

Superoxide dismutase (SOD) catalyzes the dismutation of superoxide into O_2 and H_2O_2, a remarkable process that underscores the vital role of external electron support and regulation [13]. In this reaction, the provision of two protons and an electron from an external reducing agent is essential, with metal elements such as Fe, Mn, and CuZn playing indispensable roles [14–16]. For instance, in the CuZn-catalyzed superoxide dismutation reaction, the "electron-dragging" effect of Zn^{2+} ions facilitates the reverse transfer of electrons from Cu^{+} to superoxide, ultimately generating Cu^{2+} and O_2 [17]. This regulatory mechanism of electron transfer significantly influences both the efficiency and direction of the reaction. Additionally, drawing inspiration from biological nitrogen fixation systems, Sun et al. synthesized a MoS_2/Mo_2C heterostructure, which facilitates efficient electron transfer from Mo_2C to the MoS_2 interface [18]. These biomimetic reactions not only enhance our understanding of electron transfer processes but also provide valuable insights and inspiration for the development of efficient electrocatalysts. This highlights the significance of external electron support and regulation in catalytic reactions.

In this study, we designed and synthesized N,S co-doped $CoFe_2O_4$/MoC heterojunction catalysts featuring abundant oxygen vacancies through a cation exchange method, which significantly enhances their electrocatalytic performance. The incorporation of nitrogen and sulfur elements facilitated selective electron-dragging regulation during the hydrogen evolution reaction (HER) and oxygen evolution reaction (OER). Furthermore, the unique coral-like structure provided efficient and rapid channels for ion transport. Density functional theory (DFT) calculations revealed that the formation of $CoFe_2O_4$/MoC heterojunctions substantially increased electron transfer quantities, and its optimized electronic structure further enhanced the selective catalytic performance for HER and OER compared to single MoC or $CoFe_2O_4$. When the N, S co-doped $CoFe_2O_4$/MoC (N, S-CFO/MC-NS) catalyst was applied to both the cathode and anode of alkaline electrolyzers, efficient and stable electrocatalytic performance was achieved. This study not only elucidates catalytic behaviors consistent with natural electron-dragging mechanisms but also provides novel theoretical and experimental perspectives for the design and optimization of high-performance electrocatalysts.

2. Experimental section

2.1. Synthesis of N, S-Fe_2O_3

A 1 cm × 1 cm piece of nickel foam (NF) was subjected to ultrasonic cleaning in a 3 M HCl solution for 2 h. The sample was then rinsed separately with acetone (C_3H_6O) and deionized water for 30 min each, followed by drying for subsequent use. Next, 2 mmol of $Fe(NO_3)_3{\cdot}9H_2O$ and 2 mmol of CH_4N_2O were dissolved in 35 mL of deionized water and stirred until a homogeneous solution was achieved. This solution was poured into a 50 mL reaction vessel, into which the pretreated NF was placed vertically. The vessel was then maintained at 150 °C in an oven for 6 h. After the reaction was complete, the sample was rinsed with deionized water and dried in a vacuum oven at 60 °C. Following the drying process, sulfur powder, weighing twice the amount of the loaded precursor, was added to the loaded NF and placed in a nitrogen atmosphere, maintaining the temperature at 350 °C for 2 h. The final product obtained was N, S-doped Fe_2O_3 (**N,S-Fe_2O_3**).

2.2. Synthesis of N, S-$CoMoO_4$ (N,S-CMO)

A 1 cm × 1 cm piece of nickel foam (NF) was subjected to ultrasonic cleaning in a 3 M HCl solution for 2 h. The sample was then rinsed separately with acetone (C_3H_6O) and deionized water for 30 min each, followed by drying for subsequent use. Next, 2 mmol of $Co(NO_3)_2{\cdot}6H_2O$, 2 mmol of $(NH_4)_6Mo_7O_{24}{\cdot}4H_2O$, and 2 mmol of CH_4N_2O were dissolved in 35 mL of deionized water and stirred until a homogeneous solution was achieved. This solution was poured into a 50 mL reaction vessel, into which the pretreated NF was placed vertically. The vessel was then maintained at 150 °C in an oven for 6 h. Upon completion of the reaction, the sample was rinsed with deionized water and dried in a vacuum

oven at 60 °C. Following the drying process, sulfur powder, weighing twice the amount of the loaded precursor, was added to the loaded NF and placed in a nitrogen atmosphere, with the temperature maintained at 350 °C for 2 h. The final product obtained was N,S-$CoMoO_4$ (N,S-CMO).

2.3. Synthesis of N, S-$CoFe_2O_4$/MoC Nanoflakes (N,S-CFO/MC-NS)

A 1 cm × 1 cm piece of nickel foam (NF) was subjected to ultrasonic cleaning in a 3 M HCl solution for 2 h. The sample was then rinsed separately with acetone (C_3H_6O) and deionized water for 30 min each, followed by drying for subsequent use. Next, 2 mmol of $Co(NO_3)_2{\cdot}6H_2O$, 2 mmol of $(NH_4)_6Mo_7O_{24}{\cdot}4H_2O$, and 2 mmol of CH_4N_2O were dissolved in 35 mL of deionized water and stirred until a homogeneous solution was achieved. This solution was poured into a 50 mL reaction vessel, into which the pretreated NF was placed vertically. The vessel was maintained at 150 °C in an oven for 6 h. Following the reaction, the sample was rinsed with deionized water and dried in a vacuum oven at 60 °C, resulting in the formation of the CMO/NF precursor. Subsequently, 1.5 mmol of $Fe(NO_3)_3{\cdot}9H_2O$ and 1.5 mmol of CH_4N_2O were dissolved in 20 mL of deionized water and 20 mL of ethanol solution. This mixture was then poured into a 50 mL reaction vessel, where the loaded CMO/NF precursor was placed vertically. The reaction vessel was maintained at 120 °C in an oven for 8 h. Upon completion of the reaction, the sample was rinsed with deionized water and dried in a vacuum oven at 60 °C. After drying, sulfur powder, weighing twice the amount of the loaded precursor, was added to the loaded NF and placed in a nitrogen atmosphere, where the temperature was maintained at 350 °C for 2 h. The final product obtained was N,S-doped $CoFe_2O_4$/MoC nanoflakes (N,S-CFO/MC-NS).

Additionally, the supporting information provides detailed descriptions of the sources and purity of the chemicals used, as well as the characterization and measurement methods employed. It also outlines the electrochemical testing procedures and the relevant theoretical calculation methods utilized in the study.

3. Results and discussion

3.1. Electrocatalyst synthesis and characterizations

Scheme. 1a illustrates the intrinsic mechanisms of the CuZn-catalyzed superoxide dismutation reaction and the N,S-CFO/MC-NS composite material in the water splitting process. The CuZn catalyst facilitates the decomposition of superoxide (O_2^-) into O_2 and H_2O_2 by providing active sites. The metallic properties of Cu and Zn enable effective adsorption and activation of superoxide, thereby reducing the activation energy and enhancing the reaction rate. Concurrently, CuZn modulates electron distribution, optimizing electron transfer and further improving reaction efficiency. In the N,S-CFO/MC-NS composite catalyst, $CoFe_2O_4$ and MoC play crucial roles in the oxygen evolution and hydrogen evolution reactions, respectively. Nitrogen and sulfur doping optimize the electronic structure, enhancing the adsorption and

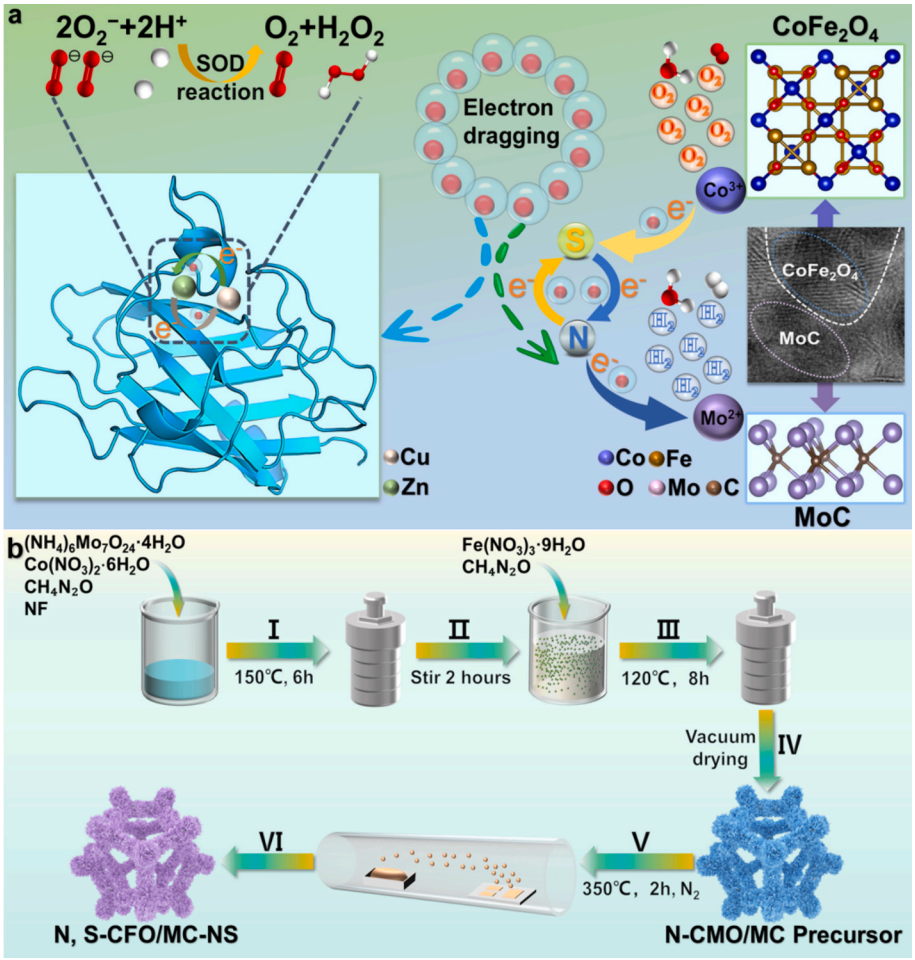

Scheme 1. a) A schematic diagram illustrating the relationship between the "electron-dragging" effect in the mechanism of superoxide disproportionation by Cu/Zn superoxide dismutase (SOD) and the catalytic mechanism of overall water decomposition by N,S-$CoFe_2O_4$/MoC-NS is presented. b) Schematic illustration of the synthesis scheme of N,S-$CoFe_2O_4$/MoC-NS.

transformation of reaction intermediates while lowering the energy barrier. In both catalysts, the modulation of the electronic structure is key to enhancing catalytic performance. CuZn optimizes the adsorption and conversion of superoxide through metal-metal synergistic effects, while the N,S-CFO/MC-NS composite material enhances the adsorption and transformation of reaction intermediates by optimizing its electronic structure. Both catalysts refine the reaction process through precise electronic structure regulation. Scheme.1b provides a detailed description of the synthesis steps for N, S-CFO/MC-NS, comprising a two-step hydrothermal reaction followed by sulfur doping. The preparation of the CMO/NF precursor resulted in the cation exchange of Fe^{2+} upon completion of the hydrothermal reaction, leading to the formation of the N-CMO/MC precursor. Subsequently, low-temperature annealing was conducted to obtain N,S-doped CMO/MC-NS while introducing oxygen vacancies. During the hydrothermal reaction, urea acted as a reducing agent, enhancing the interaction between Fe^{2+} ions in hydrated iron(III) nitrate and Co^{2+} and Mo^{6+} ions, thereby facilitating the formation of the $CoFe_2O_4$ and MoC composite. The cation exchange of iron was achieved through reduction and coordination reactions, ensuring the effective transfer of iron from the nitrate to the newly formed structure [19,20].

The morphologies of nickel foam (NF), N,S-doped Fe_2O_3, N,S-CMO, and N,S-CFO/MC-NS were examined using scanning electron microscopy (SEM) as illustrated in Fig. 1a-d. The contact angles of each sample were also measured, as shown in the inserts of the same figures. The results indicated that, in contrast to the nanoflower morphology of N,S-Fe_2O_3, N,S-CMO exhibited a coral-like nanosheet structure. This coral-like nanosheet structure was preserved in N,S-CFO/MC synthesized via cation exchange reaction, accompanied by a gradual decrease in contact angle. This observation suggests that N,S doping and the subsequent synthesis steps effectively modified the surface properties of the materials, likely significantly influencing their catalytic performance and surface hydrophilicity. Furthermore, by analyzing the SEM images of N,S-CFO/MC-NS at various magnifications, we found that the layered nanosheet structure provided efficient pathways for ion transport during the water electrolysis process. This layered structure not only facilitated the rapid migration of ions but also enhanced catalytic efficiency by increasing the effective reaction area of the catalyst. Additionally, the ample space helped mitigate unnecessary collisions caused by volume changes during the electrochemical reaction process, thereby reducing deformation of the catalyst. These structural characteristics impart significant flexibility and stability to the catalytic electrode, ensuring more durable catalytic performance in practical applications [21,22]. Numerous exposed fine nanoparticles were observed on the surface of N, S-CFO/MC-NS, which not only increased the catalyst's surface area and provided additional active sites but also potentially introduced extra charge transfer pathways by forming heterojunction interfaces. This phenomenon may lower the energy barriers for both oxygen evolution and hydrogen evolution reactions, thereby enhancing catalytic performance (Fig.S1, Supporting Information).

Further transmission electron microscopy (TEM) analysis confirmed the presence of thin carbon layers (Fig. 1e-g). The high-resolution transmission electron microscopy (HRTEM) image of N,S-CFO/MC-NS revealed lattice fringes corresponding to $CoFe_2O_4$ and MoC, with interplanar distances of 0.49 nm and 0.27 nm, respectively, which correspond to the $CoFe_2O_4$ (111) plane and MoC (001) plane (Fig. 1h). The slight increase in interplanar spacing may be attributed to the formation of oxygen vacancies, leading to the rearrangement of surrounding atoms. The absence of oxygen atoms can cause adjacent metal ions in the crystal structure to separate due to the lack of oxygen coordination, resulting in lattice expansion [23–25]. The light red boundary region between $CoFe_2O_4$ and MoC illustrated in Fig. 1h clearly indicates the formation of a heterogeneous structure. The numerous defects observed in the white region suggest a potential presence of oxygen

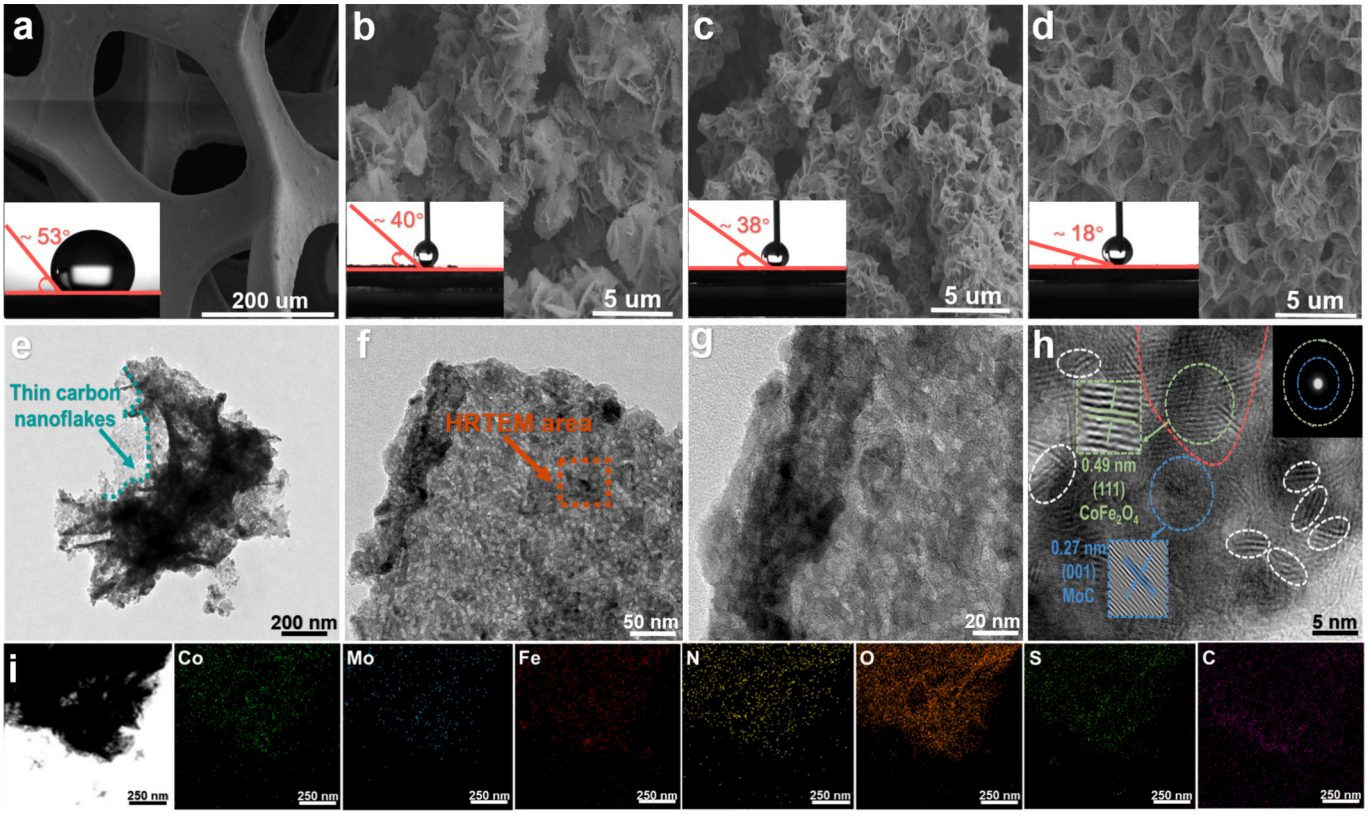

Fig. 1. a) SEM image of pure nickel foam. b) SEM image of N,S-Fe_2O_3. c) SEM image of N,S-CMO. d) SEM image of N,S-CFO/MC-NS. e-g) TEM images of N,S-CFO/MC-NS at different magnifications. h) HRTEM image of N,S-CFO/MC-NS, with the inset showing the selected area electron diffraction pattern. i) Elemental mapping of Co, Mo, Fe, N, O, S, and C of N,S-CFO/MC-NS.

vacancies. Furthermore, the selected area electron diffraction (SAED) pattern presented in Fig. 1h confirms that N,S-CFO/MC-NS is well crystallized. Atomic force microscopy (AFM) measurements indicate that the average thickness of the nanosheets is approximately 7 nm (Fig. S2, Supporting Information). Additionally, energy dispersive spectroscopy (EDS) analysis of N,S-CFO/MC-NS reveals a uniform distribution of Co, Mo, Fe, N, O, S, and C elements (Fig. 1i).

The presence of crystalline phases during sample preparation was confirmed through X-ray diffraction (XRD). The N,S-CFO/MoC-NS samples were synthesized using a two-step hydrothermal sulfidation method, while N,S-CMO and N,S-Fe_2O_3 were synthesized using similar methodologies (details can be found in the experimental section). In the N,S-CFO/MC samples synthesized on a nickel foam (NF) substrate, significant diffraction peaks corresponding to $CoFe_2O_4$ (PDF#03–0864) and MoC (PDF#45–1015) were prominently observed, particularly the 220, 311, and 511 diffraction peaks of $CoFe_2O_4$ at 30°, 35°, and 57°, respectively (Fig. 2a). A further comparison of the XRD patterns of N,S-Fe_2O_3 revealed characteristic diffraction peaks of NiS (PDF#12–0041) on the nickel foam substrate, indicating that the sulfur element primarily entered the samples in a doped form during the sulfidation process (Fig. S3-a, Supporting Information) [26]. To further confirm the structural characteristics of the catalyst, Raman spectroscopy tests were conducted. The results indicated that, compared to N,S-Fe_2O_3 and N,S-CMO, the N,S-CFO/MC exhibited characteristic peaks at 360, 660, and 940 cm^{-1}, corresponding to Co-O-Fe, Fe—Co, and MoC, respectively (Fig.S3-b, Supporting Information) [27–29]. X-ray absorption near-edge structure (XANES) spectra indicate that the cobalt element in N,S-CFO/MC-NS has an absorption edge that is slightly higher than that of N,S-CMO and Co$(OH)_2$, but lower than that of Co_3O_4 (Fig. 2b). This observation suggests that, following the cation exchange reaction, the average oxidation state

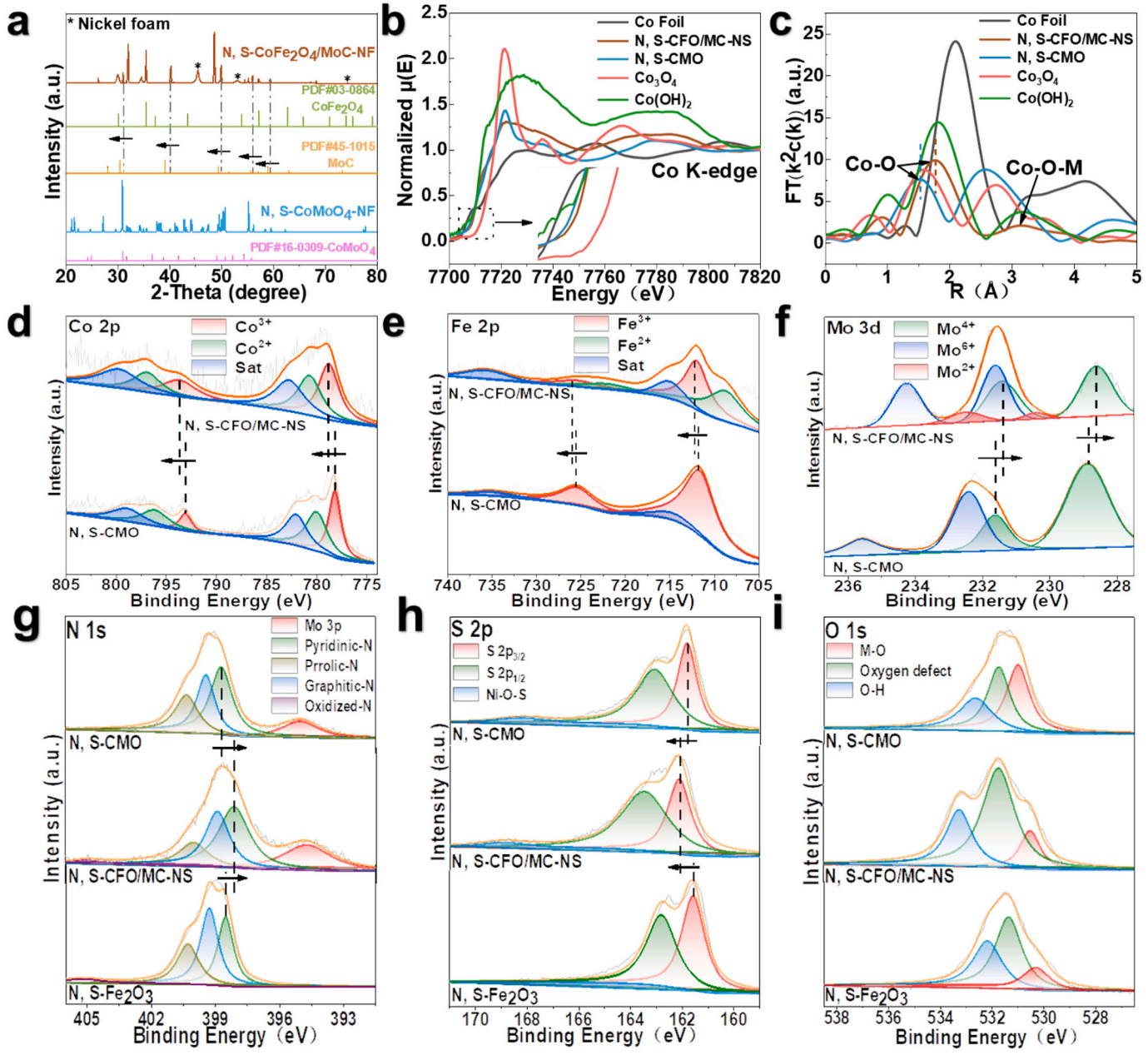

Fig. 2. a) XRD results of N,S-CFO/MC-NS and N, S-CMO. b) XANES spectra of the K-edge of Co element in N,S-CFO/MC-NS. c) Fourier transform results of the XANES spectra of the K-edge of Co element in N,S-CFO/MC-NS. d) Co 2p XPS spectra of N,S-CFO/MC-NS and N,S-CMO. e) Fe 2p XPS spectra of N,S-CFO/MC-NS and N,S-Fe_2O_3. f) Mo 3d XPS spectra of N,S-CFO/MC-NS and N,S-CMO. g) N 1 s XPS spectra of N,S-CFO/MC-NS, N,S-CMO, and N,S-Fe_2O_3. h) S 2p XPS spectra of N,S-CFO/MC-NS, N,S-CMO, and N,S-Fe_2O_3. i) O 1 s XPS spectra of N,S-CFO/MC-NS, N,S-CMO, and N,S-Fe_2O_3.

of cobalt in N,S-CFO/MC-NS is approximately Co^{2+}. Furthermore, Fourier-transform extended X-ray absorption fine structure (FT-EXAFS) spectra were utilized to examine the local electronic structure and coordination environment of cobalt in N,S-CFO/MC-NS. As illustrated in Fig. 2c, a peak at 1.75 Å corresponds to the Co—O bond in N,S-CFO/MC-NS. In comparison, the Co—O bond at 1.50 Å in N,S-CMO suggests that the longer Co—O bond in N,S-CFO/MC-NS reflects a modification in the coordination environment surrounding cobalt, likely associated with the emergence of oxygen vacancies. Additionally, contrasting the Co(OH)-O-M(OH) bond at 3.16 Å in N,S-CMO, the Co-O-M bond at 2.74 Å in N,S-CFO/MC-NS has undergone a shift, indicating a substantial alteration in the local environment around cobalt post-cation exchange. This transformation aligns with the typical octahedral coordination observed in $CoFe_2O_4$ spinel oxide. In the wavelet transform extended X-ray absorption fine structure (WT-EXAFS) spectrum, a peak corresponding to cobalt atoms in N,S-CFO/MC-NS is observed at 5.0 $Å^{-1}$ (Fig.S4-a, Supporting Information), while N, S-CMO and Co foil display peaks at 5.3 $Å^{-1}$ and 6.2 $Å^{-1}$, respectively (Fig.S4-bc, Supporting Information). The variations in the WT-EXAFS spectra further corroborate the alterations in the coordination environment surrounding cobalt following iron cation exchange [30–32]. Additionally, electron paramagnetic resonance (EPR) spectra reveal that N, S-CFO/MC-NS exhibits a more pronounced peak near around 2.0 compared to N,S-CMO, indicating an elevated concentration of oxygen vacancies (Fig.S5, Supporting Information). This observation elucidates how the presence of oxygen vacancies mitigates lattice strain, resulting in an increase in the lattice constant of MoC, which subsequently leads to a shift of the associated diffraction peaks to lower angles. Furthermore, Brunauer-Emmett-Teller (BET) surface area analysis (Fig.S6, Supporting Information) demonstrates that N,S-CFO/MC has an increase in specific surface area of nearly 20 $m^2\ g^{-1}$ compared to N,S-CMO, along with a more varied pore size distribution. This finding suggests that the cation exchange reaction positively influences the expansion of the surface area and the enhancement of defect sites. The increased surface area facilitates the dispersion of the heterostructural CFO/MC, thereby improving the utilization of active sites and promoting the transport of reactants and products during the HER and OER processes [33].

X-ray photoelectron spectroscopy (XPS) analysis further elucidated the variations in surface composition and electronic structure of the N,S-CFO/MC-NS catalyst. The comprehensive XPS survey spectrum distinctly revealed the surface elemental compositions of the N,S-CFO/MC-NS, N,S-CMO, and N,S-Fe_2O_3 catalysts (Fig. S7a).In the Co 2p spectral analysis (Fig. 2d), the N,S-CFO/MC-NS catalyst exhibited characteristic peaks for Co^{3+} at 778.8 and 793.6 eV, and for Co^{2+} at 780.8 and 796.9 eV, accompanied by lower-energy satellite peaks at 782.8 and 799.8 eV, respectively. Compared to N,S-CMO, the binding energy of Co^{3+} in the N,S-CFO/MC-NS catalyst shifted to higher energy, indicating a reduction in electron density. This shift is beneficial for enhancing the catalyst's activity in the OER [34]. Similarly, in the Fe 2p spectrum (Fig. 2e), the N,S-CFO/MC-NS catalyst displayed characteristic peaks for Fe^{2+} at 708.9 and 722.7 eV, and for Fe^{3+} at 712.2 and 725.9 eV. Additionally, satellite peaks at 715.4 and 736.1 eV corroborated the presence of Fe^{3+}. Relative to N,S-CMO, the binding energy of Fe^{3+} in the N,S-CFO/MC-NS catalyst also exhibited a shift to higher energy, potentially linked to enhanced reactivity in the formation and cleavage of O—O bonds [35]. In the Mo 3d spectral analysis (Fig. 2f), the N,S-CFO/MC-NS catalyst showed characteristic peaks for Mo^{2+} at 230.6 and 233.0 eV, peaks at 232.0 and 235.1 eV attributed to Mo^{6+}, and peaks for Mo^{4+} at 231.7 and 288.5 eV. This analysis indicates that the Mo^{4+} signal in the N,S-CFO/MC-NS catalyst shifted to lower energy compared to the Mo^{4+} peak in the N,S-CMO catalyst. This shift may be associated with an increase in electron density adjacent to the Mo atoms, thereby promoting the catalyst's activity in the HER. In the N 1 s spectrum (Fig. 2g), peaks at 394.7 eV, 398.1 eV, 398.8 eV, 400.0 eV, and 405.1 eV correspond to Mo 3p, pyridinic-N, pyrrolic-N, graphitic-N, and oxidized-N, respectively. In comparison to N,S-Fe_2O_3 and N,S-CMO, the pyridinic-N in N, S-CFO/MC-NS shifts to a lower binding energy region, thereby enhancing the reduction and oxidation capabilities of hydrogen and oxygen [36]. In the S 2p spectrum, peaks for S $2p_{3/2}$ and S $2p_{1/2}$ are observed at 162.0 eV and 163.4 eV, respectively, while the Ni-O-S peak appears at 168.9 eV. Compared to the N 1 s spectrum, the binding energy of S $2p_{3/2}$ shifts to a higher energy level, indicating that the sulfur element exhibits greater stability during the catalytic process. This stability contributes to the improved long-term durability and stability of the catalyst (Fig. 2h) [3]. In the O 1 s spectrum of N, S-CFO/MC-NS, the peaks at 530.4 eV (M-O), 531.7 eV (oxygen defect), and 533.2 eV (O—H) highlight the significant influence of oxygen defects, which is consistent with the EPR test results (Fig. 2i) [37]. Relevant studies have demonstrated that oxygen vacancies play a critical role in both the anode and cathode sides of the water splitting reaction. They enhance the electronic transfer capability of the catalytic surface by providing active sites for the adsorption and transformation of intermediates, facilitating the adsorption and conversion of oxygen intermediates, and thereby promoting the water splitting reaction. The four peaks identified in the C 1 s spectrum, located at 284.1 eV (Mo—C), 284.9 eV (C-C/C=C), 286.1 eV (C-N/C-S), and 288.6 eV (C=O), underscore the crucial role of C—S bonds in mitigating sulfur atom leaching and preventing sulfide dissolution, thereby ensuring the catalyst's high durability in alkaline electrolyte (Fig.S7b) [38].

3.2. Electrocatalytic OER performances

We first evaluated the OER performance of N,S-CFO/MC-NS in an alkaline environment. To mitigate the influence of Co^{2+} on the anodic peak, we initially assessed the overpotential from the negative scan. The polarization curves presented in Fig. 3a demonstrate that at a current density of 100 mA cm^{-2}, the overall activity of N,S-CFO/MC-NS surpasses that of N,S-CMO and N,S-Fe_2O_3, specifically indicating N,S-CFO/MC-NS (160 mV) > N,S-CMO (270 mV) > N,S-Fe_2O_3 (390 mV). Furthermore, at a current density of 300 mA cm^{-2}, the overpotential of N,S-CFO/MC-NS (217 mV) is 150 mV lower than that of N,S-CMO (367 mV). To validate the true catalytic activity of N,S-CFO/MC-NS, we compared the overpotentials obtained from both positive and negative scans and found no significant differences (Fig.S8-a, Supporting Information). Fig. 3b illustrates the Tafel slopes that reflect the reaction kinetics of the OER. The data indicate that pure NF exhibits a Tafel slope of 143 mV dec^{-1}, whereas N,S-Fe_2O_3 and N, S-CMO have Tafel slopes of 97 mV dec^{-1} and 57 mV dec^{-1}, respectively. In contrast, N, S-CFO/MC-NS demonstrates a significantly lower Tafel slope of only 46 mV dec^{-1}. This finding suggests that N,S-CFO/MC-NS predominantly governs the reaction rate during the second electron transfer step of the OER ($OH^- + OH^* \rightarrow H_2O + O^* + e^-$). A lower Tafel slope signifies enhanced reaction kinetics, indicating that this catalyst exhibits superior catalytic performance for the OER [39]. Furthermore, the double-layer capacitance (C_{dl}) values were obtained by scanning cyclic voltammetry (CV) curves at varying rates within the non-Faradaic region. The results presented in Fig. 3c indicate that N, S-CFO/MC-NS (10.4 mF cm^{-2}) > N, S-CMO (3.8 mF cm^{-2}) > N, S-Fe_2O_3 (2.6 mF cm^{-2}) > NF (2.1 mF cm^{-2}). Corresponding to the Cdl values, the electrochemical active surface area (ECSA) of N,S-CFO/MC-NS is 2.7 times, 4.0 times, and 4.9 times greater than that of N,S-CMO, N,S-Fe_2O_3, and NF, respectively (Fig.S8-b, Supporting Information). The LSV curves normalized by ECSA values demonstrate that N,S-CFO/MC-NS exhibits the highest catalytic activity, suggesting an increase in relevant active sites (Fig.S8-c, Supporting Information). The exchange current density (j_0) of N,S-CFO/MC-NS is 25.7 mA cm^{-2}, which exceeds that of N,S-CMO (18.3 mA cm^{-2}) by 7.4 mA cm^{-2} (Fig. 3d). Additionally, the Nyquist plot presented in Fig. 3e shows that NF (3.62 Ω) > N,S-Fe_2O_3 (2.39 Ω) > N,S-CMO (0.35 Ω) > N, S-CFO/MC-NS (0.25 Ω). At 1.6 V (relative to RHE), the charge transfer rate of N,S-CFO/MC-NS reached 42.8 s^{-1}, surpassing that of NF (1.7 s^{-1}), N,S-Fe_2O_3 (20.1 s^{-1}), and N,S-CMO (24.8 s^{-1}) (Fig.S8-d, Supporting Information). These data indicate that the formation of the

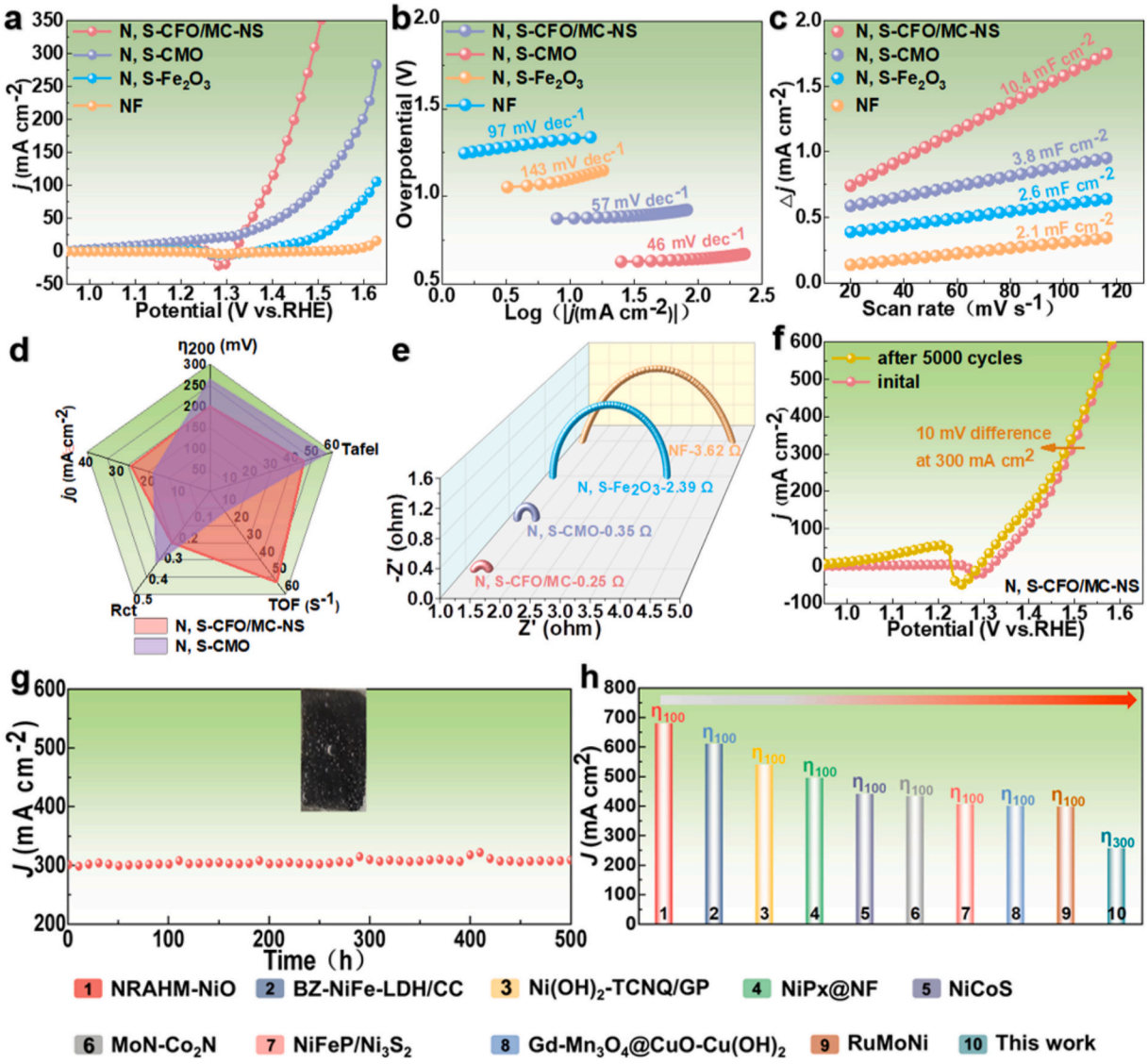

Fig. 3. OER performances of NF, N, S-Fe_2O_3, N, S-CMO, and N, S-CFO/MC-NS in 1 M KOH environment. a) LSV curves. b) Tafel plots. c) Calculated Cdl values. d) Radar chart of various performances. e) Fitted EIS spectra. f) LSV plots after 5000 CV cycles. g) Stability plot at a current density of 300 mA cm^{-2}. h) Comparison of overpotentials of N, S-CFO/MC-NS and other works.

heterostructural CFO/MC and the modulation of its dopant atoms significantly enhance catalytic activity [40]. After 5000 CV cycles, we observed an enhancement in the catalytic performance of N,S-CFO/MC-NS at a current density of 300 mA cm^{-2}. We propose that the catalyst may undergo partial reconstruction, leading to the formation of a new active phase (Fig. 3f). Concurrently, N,S-CFO/MC-NS demonstrated stable performance for 500 h at the same current density (Fig. 3g). The Faradaic efficiency, measured by the drainage method, also approached nearly 100 % (Fig.S9, Supporting Information). Contact angle tests conducted after the reaction indicated that the material surface had become nearly completely hydrophilic (Fig.S10, Supporting Information). Following the stability tests, we conducted further investigations on N, S-CFO/MC-NS. As illustrated in Fig.S11(Supporting Information), TEM images suggest that the material likely underwent partial reconstruction after the OER reaction while maintaining the integrity of the thin carbon layer. The HRTEM images (Fig.S12, Supporting Information) show that the lattice fringes in the CFO region measured 0.39 nm and 0.47 nm, which may correspond to the CoOOH (110) and FeOOH (002) planes, respectively. The heterostructure region was well-preserved, with lattice fringes of 0.25 nm and 0.27 nm corresponding to the MoC (100) and (001) planes, respectively. Energy-dispersive spectroscopy (EDS) analysis (Fig.S13, Supporting Information) revealed distinct signals for Co, Mo, Fe, N, O, S, and C, indicating the retention of relevant active sites. XPS spectra obtained post-reaction provide valuable insights into the changes in the valence states of the involved elements. The Co 2p spectrum, as shown in Fig. S14-a (Supporting Information), illustrates that the Co^{3+} peaks at 778.8 eV and 793.6 eV shifted to higher energy regions following the OER. Similarly, the Fe^{3+} peaks at 712.2 and 725.9 eV also exhibited shifts to higher energy regions (Fig.S14-b, Supporting Information). This phenomenon may be attributed to the increased oxidation states of Co^{3+} and Fe^{3+} during the reaction. Generally, such shifts are associated with an increase in charge density or alterations in oxidation states. In contrast, the Mo 3d spectrum depicted in Fig. S14-c (Supporting Information) indicates that the Mo^{2+} peaks at 230.6 eV and 233.0 eV shifted to lower energy regions, suggesting that Mo underwent reduction or an increase in electron density during the OER. This shift may result from the interaction of Mo with its surrounding environment, such as oxides in alkaline media or other dopant elements, leading to electron redistribution. The N and S elements, which modulate the electronic structure, also underwent notable changes. In the N 1 s spectrum presented in Fig. S14-d (Supporting Information) the Pyridinic-N peak at 397.8 eV shifted

to a lower energy, indicating that nitrogen gained electrons during the reaction, resulting in an increase in electron density. This increase may stem from charge transfer with the surrounding environment or interactions with neighboring metal centers, placing nitrogen in a more reduced state. In the S 2p spectrum (Fig.S14-e, Supporting Information), the S $2p_{3/2}$ peak shifted to 162.3 eV, moving to a higher energy region post-reaction, which may reflect changes in chemical bonding between sulfur and other elements (such as carbon) in the surrounding material. Similarly, the C—S bonds in the C 1 s spectrum (Fig.S14-f, Supporting Information) remained intact after the reaction, potentially helping to prevent the loss or desorption of sulfur under high oxidation conditions [41–43]. Furthermore, to highlight the superior OER performance of N, S-CFO/MC-NS, we further compared its performance with that of other catalysts in Fig. 3h.

3.3. Electrocatalytic HER performances

We assessed the HER performance in a 1 M KOH environment to investigate the bifunctional water-splitting capability. The HER polarization curves (LSV) presented in Fig. 4a indicate that the overpotentials required to achieve a current density of 100 mA cm^{-2} were 370 mV for NF, 252 mV for N,S-Fe_2O_3, 142 mV for N,S-CMO, and only 83 mV for N, S-CFO/MC-NS. At a current density of 300 mA cm^{-2}, the overpotential for N,S-CMO was 230 mV, while N,S-CFO/MC-NS exhibited the lowest overpotential of 142 mV among all the prepared catalysts. The minimal difference of only 3 mV between the anodic and cathodic scans of the LSV curve at a current density of 300 mA cm^{-2} further confirms the superior catalytic activity of N,S-CFO/MC-NS (Fig.S15-a, Supporting Information). Fig. 4b illustrates the Tafel slopes corresponding to the different LSV curves. It is evident that N,S-CFO/MC-NS has a Tafel slope of only 24.9 mV dec^{-1}, in contrast to 101.2 mV dec^{-1} for NF, 96.4 mV dec^{-1} for N,S-Fe_2O_3, and 74.4 mV dec^{-1} for N,S-CMO. This suggests that the catalytic behavior of N,S-CFO/MC-NS is primarily governed by the Tafel step (i.e., H_2 desorption) rather than the Volmer step (i.e., H_2O dissociation) as the rate-determining step. CV curves scanned at various rates within the non-Faradaic region yielded surface charge densities for evaluating Cdl. As illustrated in Fig. 4c, the C_{dl} values for NF, N,S-Fe_2O_3, and N,S-CMO were 3.4, 6.2, and 7.3 mF cm^{-2}, respectively, while N,S-CFO/MC-NS reached 9.2 mF cm^{-2}. Consequently, the assessment of the ECSA indicated that the ECSA of N,S-CFO/MC-NS was 1.25 times greater than that of N,S-CMO, suggesting an increased exposure of active sites following the cation exchange reaction (Fig.S15-b, Supporting

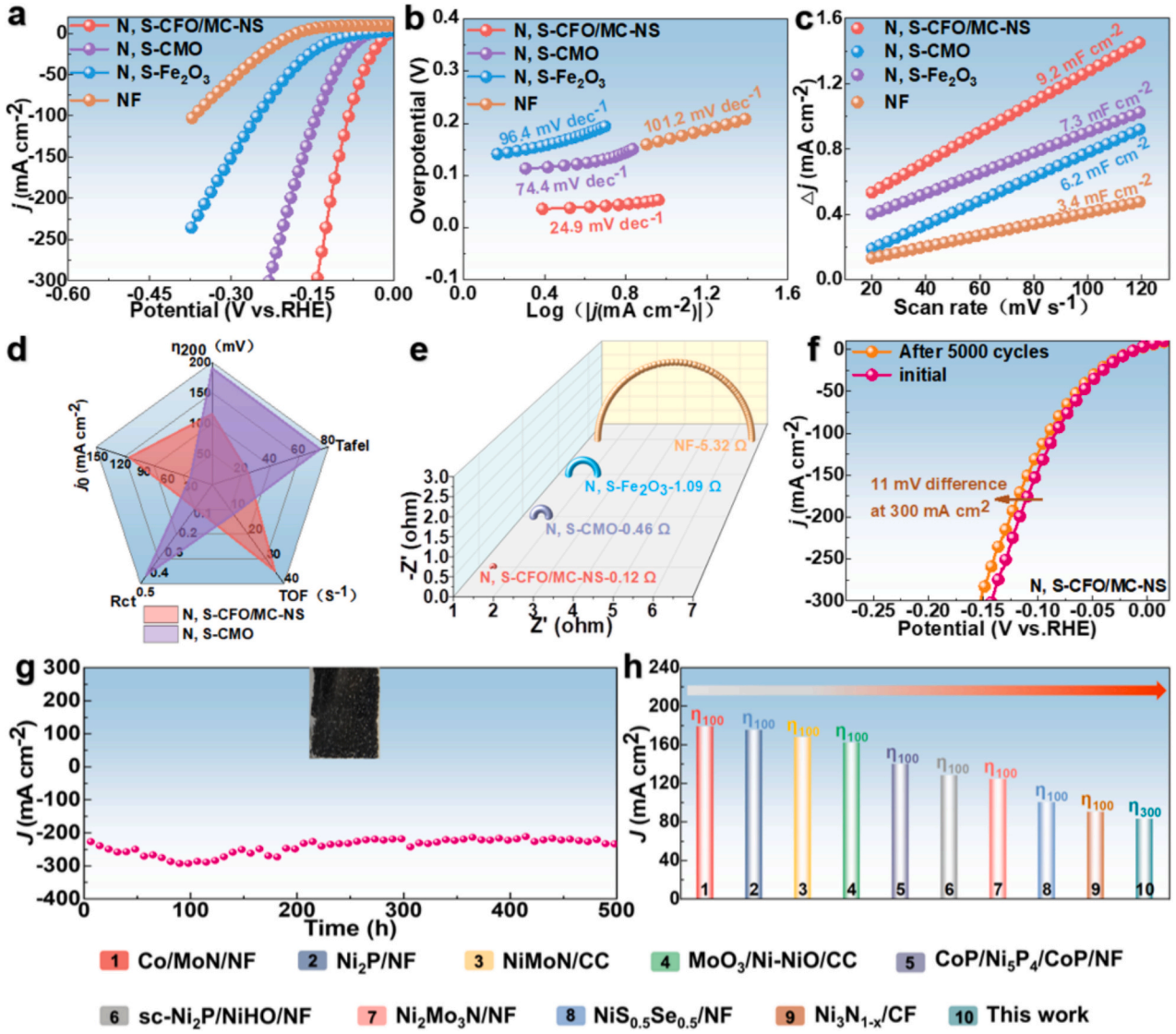

Fig. 4. HER performances of NF, N, S-Fe_2O_3, N, S-CMO, and N, S-CFO/MC-NS in 1 M KOH environment. a) LSV curves. b) Tafel plots. c) Calculated Cdl values. d) Radar chart of various performances. e) Fitted EIS spectra. f) LSV plots after 5000 CV cycles. g) Stability plot at a current density of 200 mA cm^{-2}. h) Comparison of overpotentials of N, S-CFO/MC-NS and other works.

Information). Further normalization of the LSV curves based on ECSA demonstrated that the formation of the heterostructure significantly enhanced intrinsic catalytic activity (Fig.S15-c, Supporting Information). Fig. 4d shows that the exchange current density (j_0) for N,S-CFO/MC-NS was 3.8 times higher than that of N,S-CMO, underscoring the importance of heteroatom modulation in improving the activity of the heterostructure. Additionally, the electrochemical impedance spectra (Nyquist plots) revealed that the impedance of N,S-CFO/MC-NS was only 0.12 Ω, in contrast to 5.32 Ω for NF, 1.09 Ω for N,S-Fe_2O_3, and 0.46 Ω for N,S-CMO, further corroborating the enhanced electron transfer efficiency of N,S-CFO/MC-NS in HER catalytic behavior (Fig. 4e) [44]. By comparing the turnover frequency (TOF) values at an overpotential of 200 mV (vs. RHE), we observed that the TOF values for NF, N,S-Fe_2O_3, N,S-CMO, and N,S-CFO/MC-NS were 2.9, 12.7, 14.6, and 35.5 s^{-1}, respectively (Fig.S15-d, Supporting Information). The stability of the catalyst underscores the potential of N,S-CFO/MC-NS for practical applications, which we assessed using two methods. Fig. 4f illustrates that after 5000 cycles of CV, the LSV curve for N, S-CFO/MC-NS exhibited an increase of only 11 mV at a current density of 300 mA cm^{-2}. Fig. 4g demonstrates that N,S-CFO/MC-NS can maintain stable current output for up to 500 h at a current density of 200 mA cm^{-2}.

The Faradaic efficiency, measured via the drainage method, approached nearly 100 % (Fig.S16, Supporting Information). Post-reaction contact angle measurements indicated that the material surface transitioned to a nearly completely hydrophilic state (Fig.S17, Supporting Information). Following stability tests, we conducted further investigations on N, S-CFO/MC-NS. TEM images presented in Fig.S18 (Supporting Information) suggest that the catalyst surface may have undergone partial reconstruction after the reaction. HRTEM images shown in Fig.S19 (Supporting Information) reveal lattice fringe spacings of 0.25 nm and 0.18 nm, corresponding to the $CoFe_2O_4$ (113) and MoC (101) planes, respectively [45]. The EDS spectrum in Fig.S20 (Supporting Information) confirmed that the elements Co, Mo, Fe, N, S, and C remained uniformly distributed even after the reaction. Notably, the presence of sulfur in the EDS spectrum indicates that a thin carbon layer may have inhibited the leaching of sulfur atoms, thereby enhancing the catalyst's lifespan. Moreover, XPS provided insights into the electron transfer between relevant atoms. Following the HER, the Co 2p spectrum revealed that the Co^{3+} peaks at 778.8 and 793.6 eV shifted to lower energy regions (Fig.S21-a, Supporting Information). Similarly, the Fe 2p spectrum demonstrated a shift of the Fe^{3+} peaks at 708.9 and 722.7 eV to lower energy regions (Fig.S21-b, Supporting Information). These shifts of Co^{3+} and Fe^{3+} to lower energy levels indicate that both elements may have experienced an increase in charge density or enhanced interactions with other elements (e.g., oxygen), resulting in a greater number of electrons being drawn toward lower energy states. Interestingly, the Mo 3d spectrum in Fig.S21-c (Supporting Information) indicated that the Mo^{2+} peaks at 230.6 and 233.0 eV shifted to higher energy regions. This suggests that Mo may have undergone a change in oxidation state or a redistribution of electron density during the HER reaction, potentially due to interactions with other elements or molecules in the alkaline medium. The N 1 s spectrum in Fig.S21-d (Supporting Information) also exhibited a shift of the pyridinic-N peak at 398.5 eV to a higher energy region, implying a change in the electronic structure of nitrogen atoms, likely resulting from enhanced interactions with adjacent carbon or metal atoms, which leads to local changes in electron density. Furthermore, the peak in the S $2p_{3/2}$ spectrum at 161.8 eV shifted to a lower energy region, indicating that sulfur atoms may have experienced an increase in electron density during the reaction. This could be associated with the partial reduction of sulfur atoms or relaxation of their electronic environment (Fig.S21-e, Supporting Information). Additionally, the C—S bond in the C 1 s spectrum remained intact following the reaction, suggesting that the C—S bond may play a crucial role in preventing the loss of sulfur atoms and ensuring stability (Fig. S21-f, Supporting Information) [46,47]. Additionally, we compared the performance of N,S-CFO/MC-NS with that of other catalysts, as shown in Fig. 4h, underscoring its exceptional HER performance.

3.4. Mechanism investigation

To determine the potential sources of active sites in various reaction scenarios of the OER and HER, we investigated the structural evolution of the N,S-CFO/MC-NS electrode using in situ Raman spectroscopy in a 1 M KOH environment at different open circuit voltages. Initially, we examined the dynamic changes of N,S-CFO/MC-NS as the anode during the OER process. As depicted in Fig. 5a, three distinct signal peaks at 425 cm^{-1}, 561 cm^{-1}, and 950 cm^{-1} were observed in the voltage range of 1.0 V to 1.5 V, with the peak intensities gradually increasing, indicating the formation of CoOOH species. Prior studies have demonstrated that when Co sites in $CoFe_2O_4$ participate in the OER, the reaction pathway tends to favor the adsorbate evolution mechanism (AEM). This observation suggests that Co exhibits a strong capacity to adsorb and desorb water molecules, which is crucial for enhancing both the efficiency and stability of the OER [48]. When N,S-CFO/MC-NS is employed as the cathode, we assessed its capacity to adsorb H_2O by investigating the transition from the non-Faradaic region to the HER region within the voltage range of +0.3 V to −0.2 V (vs. RHE). The in-situ Raman spectra presented in Fig. 5b clearly display a significant vibrational peak at 1635 cm^{-1}. Within the voltage range of +0.3 V to 0 V, the peak intensity progressively increased, indicating a substantial enhancement in H_2O adsorption on the N,S-CFO/MC-NS electrode surface. This increase in adsorption intensity is thought to facilitate the Volmer step by providing an adequate supply of hydrogen atoms for subsequent reactions, specifically the Tafel step, thereby enhancing the overall reaction rate and catalytic performance. Conversely, in the voltage range of 0 V to −0.3 V, a gradual decline in the vibrational intensity at 1635 cm^{-1} was observed, suggesting that water molecules may have undergone a dissociation process, with some potentially converting into hydrogen atoms or hydroxide ions, which leads to the weakening of this vibrational mode. This leads to a weakening of this vibrational mode. This observation indicates a shift in the chemical environment of the water molecules, further corroborating their involvement in the reaction mechanism [49].

Density Functional Theory (DFT) calculations were employed to further explore the potential for enhanced activity of the heterostructural $CoFe_2O_4$/MoC during the OER and HER processes. Initially, atomic structure models of $CoFe_2O_4$, MoC, and the heterostructural $CoFe_2O_4$/MoC were established and optimized. (Fig.S22, Supporting Information). The work function calculations indicated that the work functions for $CoFe_2O_4$ and MoC are 4.91 eV and 5.23 eV, respectively (Fig.S23, Supporting Information). Notably, the work function of the heterostructural $CoFe_2O_4$/MoC is 4.76 eV. This lower work function suggests that the heterostructure exhibits enhanced electron transfer capabilities, facilitating the movement of electrons from the catalyst to the reactants during the OER and HER processes, thereby promoting these reactions (Fig. 5c). Furthermore, calculations for the $CoFe_2O_4$ structural model revealed an electron transfer number of 7.3 e^-, while that for MoC was 11.6 e^-. In the charge density difference analysis of the heterostructural $CoFe_2O_4$/MoC, the electron transfer on the $CoFe_2O_4$ side was measured at 7.9 e-, while on the MoC side it was 13.3 e^-. These results indicate that the formation of the heterostructure involves a greater number of electrons in the reactions. The accumulation of charge in the yellow region and the depletion of charge in the cyan region further illustrate that the heterostructure area establishes pathways for rapid electron transport (Fig. 5d). According to the d-band center theory, the adsorption of reaction intermediates on the catalyst surface is closely related to the electron density near the Fermi level (E_F). Fig. 5e demonstrates that the heterostructural $CoFe_2O_4$/MoC is situated closer to E_F compared to $CoFe_2O_4$ and MoC, thereby enhancing the heterostructure's capacity to adsorb oxygen intermediates (such as *O and *OH) during the OER. Similarly, for the HER, this proximity increases the ability of $CoFe_2O_4$/MoC to adsorb hydrogen intermediates (such as

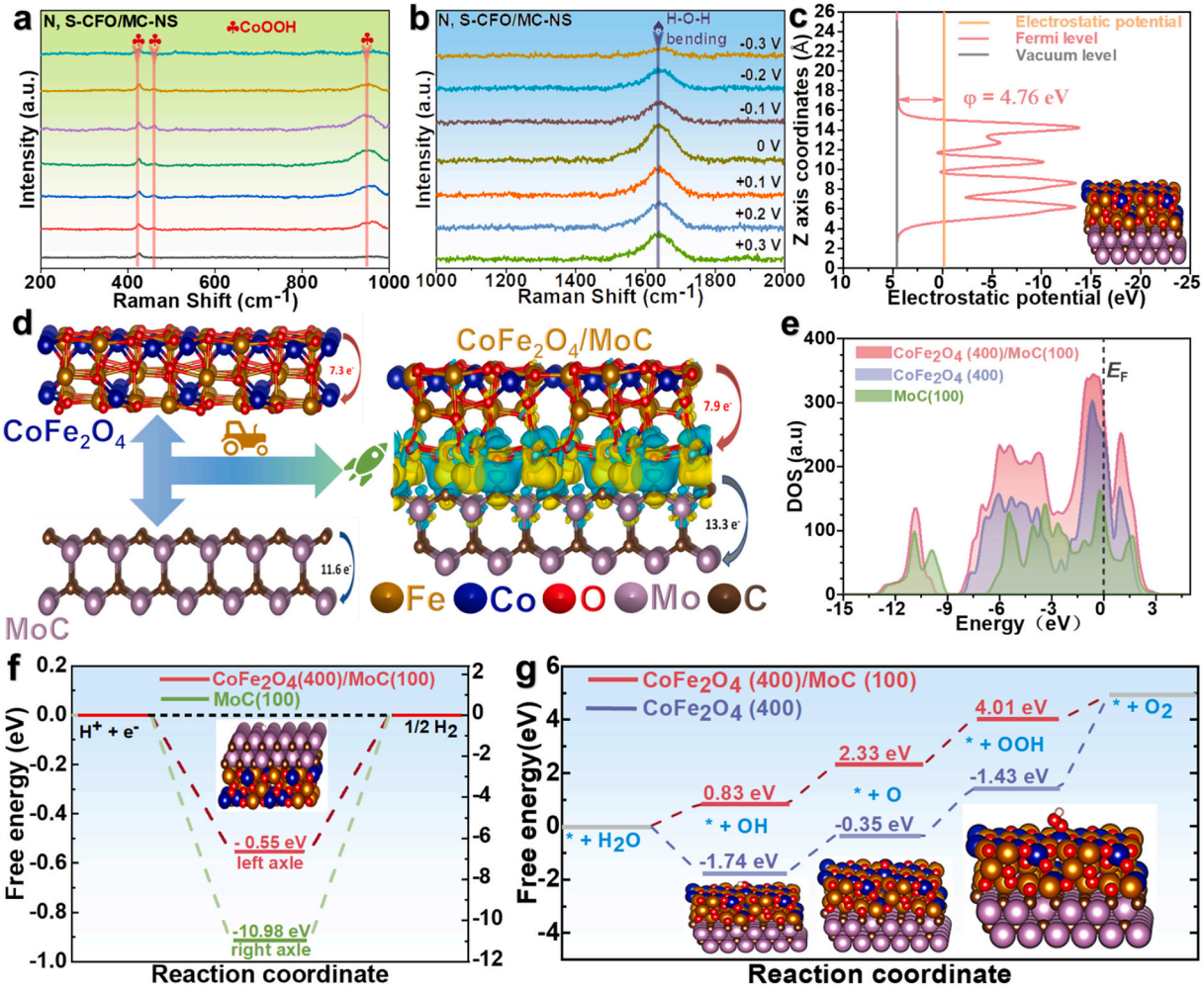

Fig. 5. a) In situ Raman spectra of N, S-CFO/MC-NS measured for OER in a 1 M KOH environment. b) In situ Raman spectra of N, S-CFO/MC-NS measured for HER in a 1 M KOH environment. c) Calculated work function (φ) of $CoFe_2O_4$/MoC. The inset shows the static geometric configuration of $CoFe_2O_4$/MoC. d) Charge density difference and Bader charge transfer at the interfaces of $CoFe_2O_4$, MoC, and $CoFe_2O_4$/MoC. The yellow and cyan regions represent charge accumulation and depletion, respectively. The golden yellow, dark green, red, light purple, and dark brown represent Fe, Co, O, Mo, and C elements, respectively. e) DOS plots of $CoFe_2O_4$, MoC, and $CoFe_2O_4$/MoC. f) Gibbs free energy diagrams of hydrogen adsorption on MoC and $CoFe_2O_4$/MoC. The inset shows the geometric configuration of H* adsorbed on the $CoFe_2O_4$/MoC structure. g) Gibbs free energy curves of OER at 1.23 V for $CoFe_2O_4$ and $CoFe_2O_4$/MoC. The inset depicts the geometric configurations of *OH, *O, and *OOH adsorbed on the $CoFe_2O_4$/MoC structure. (For interpretation of the references to colour in this figure legend, the reader is referred to the web version of this article.)

H*). This enhanced adsorption capacity can facilitate hydrogen generation, thereby improving the efficiency of the HER process. The Gibbs free energy analysis provides further insights into the understanding of various reaction pathways. As illustrated in Fig. 5f, the hydrogen free energy (ΔG_{H^*}) value for pure MoC is −10.98 eV, indicating a very strong interaction between H* and the MoC surface. This strong interaction may lead to excessive adsorption of reaction intermediates, which could hinder hydrogen release and reduce catalytic activity. In contrast, the ΔG_{H^*} value for the heterostructural $CoFe_2O_4$/MoC is −0.55 eV, which is close to the ideal value. This suggests that the adsorption energy of H* on this structure is moderate, thereby promoting hydrogen generation and release. The OER free energy profiles depicted in Fig. 5g show that both $CoFe_2O_4$ and the heterostructural $CoFe_2O_4$/MoC undergo an endothermic (uphill) process during the reaction. Notably, during the potential-determining step (PDS) for the generation of O_2 from *OOH, the energy barrier for $CoFe_2O_4$ is −1.43 eV, while for $CoFe_2O_4$/MoC, it is 4.01 eV, with the overall energy barrier for O_2 generation being 4.90 eV. This further elucidates that the formation of the heterostructure positively contributes to the OER reaction [50,51].

The analyses reveal a similar “electron-dragging” mechanism between heteroatom doping and the superoxide disproportionation reaction catalyzed by CuZn. During the OER, XPS analysis showed that Co^{3+} peaks shifted to higher energy, indicating an increased oxidation state of Co. In situ Raman spectroscopy detected CoOOH, implying that cobalt oxides or hydroxides act as active catalysts in oxygen evolution. The generation of CoOOH indicates that Co serves as an active site, interacting with water molecules or OH^- ions to facilitate oxygen generation. A similar mechanism is observed in the HER in alkaline environments. The Volmer reaction occurs first, where H^+ ions are adsorbed onto the catalyst's active sites, forming adsorbed hydrogen ($H_3O^+ + * + e^- \rightarrow H^* + H_2O$). In situ Raman analysis revealed the adsorption of water molecules on the surface of the N,S-doped $CoFe_2O_4$/MoC electrode, while XPS displayed a shift of Mo^{2+} peaks to lower energy. This shift indicates that MoC provides electrons more readily, enhancing H^+ reduction to produce H_2. This electron transfer is analogous to the CuZn-catalyzed superoxide reduction, where electron density facilitates the reduction process. DFT demonstrated that the heterostructural $CoFe_2O_4$/MoC further promotes electron transfer. The interaction decreases electron density on Co within $CoFe_2O_4$ while increasing it on Mo in MoC, thereby enhancing electron mobility. The N,S-doped heterostructural

$CoFe_2O_4$/MoC plays dual catalytic roles: improving OER via electron dragging and enhancing HER efficiency through improved electron transfer. These findings underscore the universality and significance of the electron-dragging effect in catalysis, where modulation of electron density enhances electron mobility and reaction efficiency across diverse catalytic systems.

3.5. Overall hydrolysis performances

Given the excellent performance of the N,S-CFO/MC-NS self-supporting electrode in both HER and OER, we employed it directly as both the anode and cathode in an alkaline water electrolysis cell (Fig. 6a), utilizing 1 M KOH as the electrolyte. Fig. 6b presents a comparison of the performance between the N,S-CFO/MC-NS (−) || N,S-CFO/MC-NS (+) system and the Pt/C (−) || RuO_2 (+) system. The results indicate that the N,S-CFO/MC-NS (−) || N,S-CFO/MC-NS (+) system requires a voltage of 1.47 V, while the Pt/C (−) || RuO_2 (+) system necessitates a voltage of 1.70 V, demonstrating a reduction of 0.23 V to achieve a current density of 100 mA cm^{-2}. Furthermore, to evaluate its overall durability, we conducted a long-term output test at a current density of 100 mA cm^{-2} for 300 h, confirming that the N, S-CFO/MC-NS (−) || N, S-CFO/MC-NS (+) system exhibits excellent stability (Fig. 6c). In a similar vein, we performed a comparative analysis of the battery voltages evaluated with alternative catalysts to underscore the advantages of the N,S-CFO/MC-NS (−) || N,S-CFO/MC-NS (+) system (Fig. 6d).

4. Conclusion

Inspired by the electron-polarizing mechanism observed in nature, we have successfully developed N, S-$CoFe_2O_4$/MoC-NS (N, S-CFO/MC-NS) via a cation exchange method, resulting in electrodes that demonstrate high efficiency and stability for both the OER and HER under alkaline conditions. In the $CoFe_2O_4$/MoC heterostructure, the positive modulation of N and S doping, along with the presence of oxygen vacancies, allows it to operate as an OER electrode with an overpotential of merely 217 mV at a current density of 300 mA cm^{-2}, and as an HER electrode with an overpotential of 142 mV under identical conditions. By assembling a bipolar electrode system (N, S-CFO/MC-NS (−) || N, S-CFO/MC-NS (+)), we achieved a current density of 100 mA cm^{-2} with a cell voltage of 1.47 V, maintaining stable operation for 300 h. DFT calculations indicate that the formation of the heterostructure interface promotes electron transfer. Experimental results, along with in situ Raman analysis, further confirm the 'electron-dragging 'effect of N and S elements, selectively enhancing the active sites for both OER and HER reactions. This study integrates theoretical and experimental methodologies to elucidate the microscopic mechanism behind the 'electron-polarizing' effect, providing significant insights into the development of highly efficient and stable alkaline water electrolysis systems.

CRediT authorship contribution statement

Changcheng Lin: Writing – original draft. **Huaibao Tang:** Methodology. **Jun Xu:** Validation. **Dongmeng Chen:** Methodology. **Xueqin Zuo:** Project administration. **Qun Yang:** Data curation. **Zhong Jin:** Writing – review & editing. **Haifeng Xu:** Supervision. **Guang Li:** Formal analysis.

Declaration of competing interest

The authors declare that they have no known competing financial

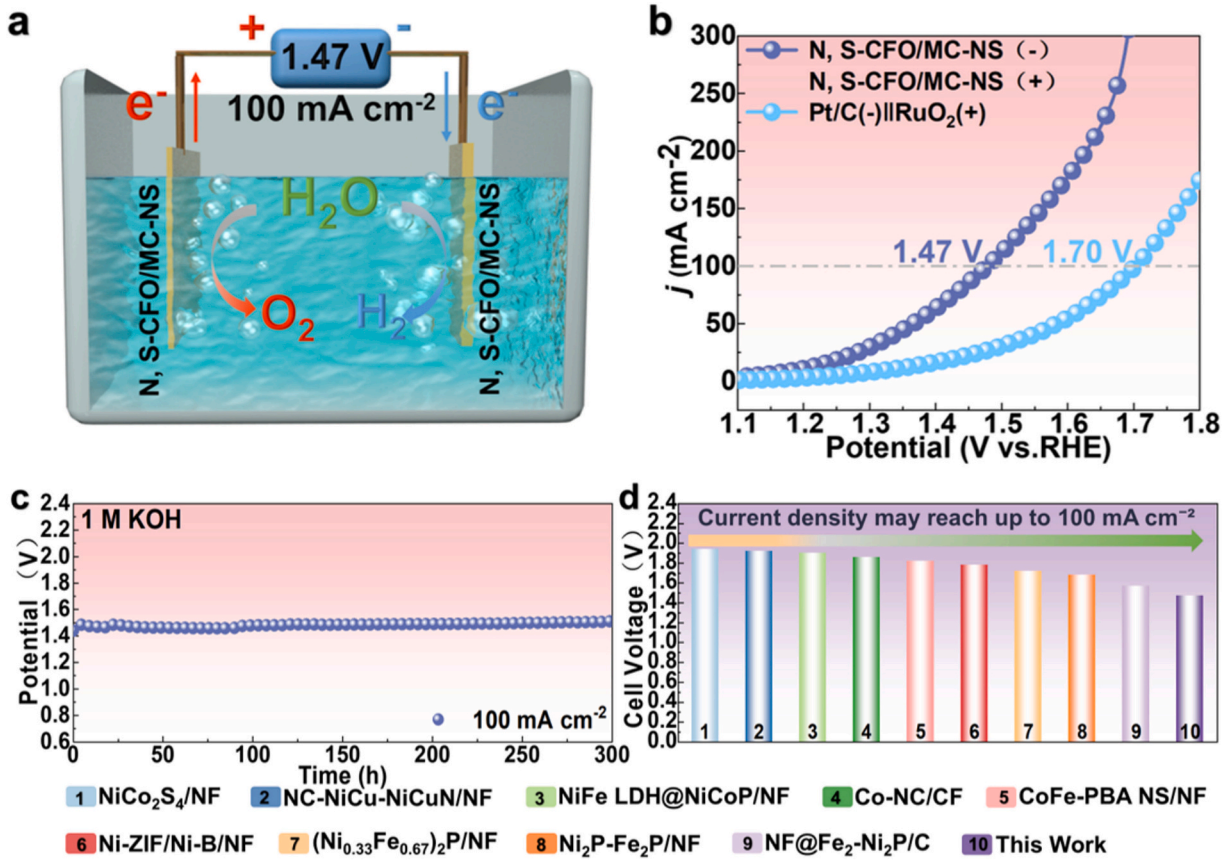

Fig. 6. a) Schematic illustration of the N, S-CFO/MC-NS (−) || N, S-CFO/MC-NS (+) electrolytic cell system. b) Polarization curves of the N, S-CFO/MC-NS (−) || N, S-CFO/MC-NS (+) and Pt/C (−) || RuO_2 (+) electrolytic cell systems. c) Chronopotentiometry (CP) test of the N, S-CFO/MC-NS (−) || N, S-CFO/MC-NS (+) electrolytic cell system at 1.47 V. d) Comparison of current density performance of N, S-CFO/MC-NS with electrolytic cells of different materials up to 100 mA cm^{-2}.

interests or personal relationships that could have appeared to influence the work reported in this paper.

Acknowledgments

This work was financially supported by the Excellent Research Innovation Team of Anhui Provincial Education Department (2023AH010001), the Recruitment Program for Leading Talent Team of Anhui Province (LTIT20200002), the National Key Research and Development Program of China (2017YFA0403503), the Key Projects of Natural Science Research in Universities of Anhui Province (No. 2023AH051314), the National Natural Science Foundation of China (22479074 and 22475096), the General Project of the Joint Fund of Equipment Pre-research and the Ministry of Education (8091B02052407), the Natural Science Foundation of Jiangsu Province (BK20240400 and BK20241236), the Science and Technology Major Project of Jiangsu Province (BG2024013), the Scientific and Technological Achievements Transformation Special Fund of Jiangsu Province (BA2023037), the Academic Degree and Postgraduate Education Reform Project of Jiangsu Province (JGKT24_C001), the Jiangsu Province Academic Degree and Postgraduate Education Reform Project (JGKT24_C001), the Key Core Technology Open Competition Project of Suzhou City (SYG2024122), the Gusu Leading Talent Program of Scientific and Technological Innovation and Entrepreneurship of Wujiang District in Suzhou City (ZXL2021273), and the Chenzhou National Sustainable Development Agenda Innovation Demonstration Zone Provincial Special Project (2023sfq11).

Appendix A. Supplementary data

Supplementary data to this article can be found online at https://doi.org/10.1016/j.jcis.2025.138249.

Data availability

Data will be made available on request.

References

[1] X. Li, X. Yang, H. Xue, H. Pang, Q. Xu, Metal–organic frameworks as a platform for clean energy applications, EnergyChem 2 (2020) 100027.
[2] X. Xiao, L. Zou, H. Pang, Q. Xu, Synthesis of micro/nanoscaled metal-organic frameworks and their direct electrochemical applications, Chem. Soc. Rev. 49 (2020) 301–331.
[3] Y. Song, X. Zhang, Z. Xiao, Y. Wang, P. Yi, M. Huang, L. Zhang, Coupled amorphous NiFeP/cystalline Ni_3S_2 nanosheets enables accelerated reaction kinetics for high current density seawater electrolysis, Appl. Catal. B Environ. 352 (2024) 124028.
[4] X. Sun, W. Shen, H. Liu, P. Xi, M. Jaroniec, Y. Zheng, S.Z. Qiao, Corrosion-resistant NiFe anode towards kilowatt-scale alkaline seawater electrolysis, Nat. Commun. 15 (2024) 10351.
[5] W. Choi, G. Park, K.L. Bae, J.Y. Choi, K.M. Nam, H. Song, Metal-semiconductor double shell hollow nanocubes for highly stable hydrogen generation photocatalysts, J. Mater. Chem. A 4 (2016) 13414–13418.
[6] S. Zhang, Y. Wang, S. Li, Z. Wang, H. Chen, L. Yi, X. Chen, Q. Yang, W. Xu, A. Wang, Z. Lu, Concerning the stability of seawater electrolysis: a corrosion mechanism study of halide on Ni-based anode, Nat. Commun. 14 (2023) 4822.
[7] H. Wang, L. Zhang, Z. Chen, J. Hu, S. Li, Z. Wang, J. Liu, X. Wang, Semiconductor heterojunction photocatalysts: design, construction, and photocatalytic performances, Chem. Soc. Rev. 43 (2014) 5234–5244.
[8] B. Dieny, I.L. Prejbeanu, K. Garello, P. Gambardella, P. Freitas, R. Lehndorff, W. Raberg, U. Ebels, S.O. Demokritov, J. Akerman, A. Deac, P. Pirro, C. Adelmann, A. Anane, A.V. Chumak, A. Hirohata, S. Mangin, S.O. Valenzuela, M.C. Onbaşlı, M. d'Aquino, G. Prenat, G. Finocchio, L. Lopez-Diaz, R. Chantrell, O. Chubykalo-Fesenko, P. Bortolotti, Opportunities and challenges for spintronics in the microelectronics industry, Nat. Electron. 3 (2020) 446–459.
[9] X.H. Li, M. Antonietti, Metal nanoparticles at mesoporous N-doped carbons and carbon nitrides: functional Mott–schottky heterojunctions for catalysis, Chem. Soc. Rev. 42 (2013) 6593–6604.
[10] Z. Xie, B. Zhang, Y. Ge, Y. Zhu, G. Nie, Y.F. Song, C.K. Lim, H. Zhang, P.N. Prasad, Chemistry, functionalization, and applications of recent Monoelemental two-dimensional materials and their Heterostructures, Chem. Rev. 122 (2022) 1127–1207.
[11] H. Zhang, H. Jin, Y. Yang, F. Sun, Y. Liu, X. Du, S. Zhang, F. Song, J. Wang, Y. Wang, Z. Jiang, Understanding the synergetic interaction within A-MoC/B-Mo_2C heterostructured electrocatalyst, J. Energy Chem. 35 (2019) 66–70.
[12] H. Yu, S. Zhu, Y. Hao, Y.M. Chang, L. Li, J. Ma, H.Y. Chen, M. Shao, S. Peng, Modulating local interfacial bonding environment of Heterostructures for energy-saving hydrogen production at high current densities, Adv. Funct. Mater. 33 (2023) 2212811.
[13] Y. Sheng, I.A. Abreu, D.E. Cabelli, M.J. Maroney, A.F. Miller, M. Teixeira, J. S. Valentine, Superoxide dismutases and superoxide reductases, Chem. Rev. 114 (2014) 3854–3918.
[14] R.R. Crichton, J.L. Pierre, Old iron, young copper: from Mars to Venus, BioMetals 14 (2001) 99–112.
[15] M.A. Saito, D.M. Sigman, F.M.M. Morel, The bioinorganic chemistry of the ancient ocean: the co-evolution of cyanobacterial metal requirements and biogeochemical cycles at the Archean-Proterozoic boundary? Inorg. Chim. Acta 356 (2003) 308–318.
[16] F.L. Sousa, T. Thiergart, G. Landan, S. Nelson-Sathi, I.A.C. Pereira, J.F. Allen, N. Lane, W.F. Martin, Early bioenergetic evolution, Philos. Trans. R. Soc. B Biol. Sci. 368 (2013) 20130088.
[17] J. Han, H. Tan, K. Guo, H. Lv, X. Peng, W. Zhang, H. Lin, U. Apfel, R. Cao, The "pull effect" of a hanging Zn^{II} on improving the four-Electron oxygen reduction selectivity with co porphyrin, Angew. Chem. Int. Ed. 136 (2024) e202409793.
[18] T. Ye, K. Ba, X. Yang, T. Xiao, Y. Sun, H. Liu, C. Tang, B. Ge, P. Zhang, T. Duan, Z. Sun, Valence engineering at the interface of MoS_2/Mo_2C heterostructure for bionic nitrogen reduction, Chem. Eng. J. 452 (2023) 139515.
[19] J.L. Fenton, R.E. Schaak, Structure-selective cation exchange in the synthesis of Zincblende MnS and CoS nanocrystals, Angew. Chem. Int. Ed. 56 (2017) 6464–6467.
[20] W. Liu, G. Long, Z. Xiang, J. Piao, K. Wan, Z. Fu, Z. Liang, Extremely active and robust Ir-Mn dual-atom Electrocatalyst for oxygen evolution reaction by oxygen-oxygen radical coupling mechanism, Angew. Chem. Int. Ed. 136 (2024) e202411014.
[21] S. Wang, Y. Wang, S.Q. Zang, X.W. Lou, Hierarchical hollow Heterostructures for photocatalytic CO_2 reduction and water splitting, Small Methods. 4 (2020) 1900586.
[22] Y. Zhu, W. Peng, Y. Li, G. Zhang, F. Zhang, X. Fan, Multiple roles of a heterointerface in two-dimensional van der Waals heterostructures: insights into energy-related applications, J. Mater. Chem. A 7 (2019) 23577–23603.
[23] B. Wang, X. Chen, Y. He, Q. Liu, X. Zhang, Z. Luo, J.V. Kennedy, J. Li, D. Qian, J. Liu, G.I.N. Waterhouse, Fe_2O_3/P-doped $CoMoO_4$ electrocatalyst delivers efficient overall water splitting in alkaline media, Appl. Catal. B Environ. 346 (2024) 123741.
[24] H. Wang, Q. Hu, J. Qiu, R. Guo, X. Liu, Research progress of spinel $CoFe_2O_4$ as an electrocatalyst for the oxygen evolution reaction, Catal, Sci. Technol. 13 (2023) 6102–6125.
[25] X. Zhou, Y. Tian, J. Luo, B. Jin, Z. Wu, X. Ning, L. Zhan, X. Fan, T. Zhou, S. Zhang, X. Zhou, MoC quantum dots@N-doped-carbon for low-cost and efficient hydrogen evolution reaction: from Electrocatalysis to Photocatalysis, Adv. Funct. Mater. 32 (2022) 2201518.
[26] J. Wang, J. Hu, C. Liang, L. Chang, Y. Du, X. Han, J. Sun, P. Xu, Surface reconstruction of phosphorus-doped cobalt molybdate microarrays in electrochemical water splitting, Chem. Eng. J. 446 (2022) 137094.
[27] M. Chen, C. Song, C. Liang, B. Zhang, Y. Sun, S. Li, L. Lin, P. Xu, Crystalline phase induced Raman enhancement on molybdenum carbides, Inorg. Chem. Front. 9 (2022) 2575–2582.
[28] M. Kamranifar, A. Allahresani, A. Naghizadeh, Synthesis and characterizations of a novel $CoFe_2O_4$@CuS magnetic nanocomposite and investigation of its efficiency for photocatalytic degradation of penicillin G antibiotic in simulated wastewater, J. Hazard. Mater. 366 (2019) 545–555.
[29] Y. Wang, J. Shi, Z. Zhang, J. Fu, X. Lü, Z. Hou, Carbon film encapsulated Fe_2O_3: an efficient catalyst for hydrogenation of nitroarenes, Cuihua Xuebao/Chinese, J. Catal. 38 (2017) 1909–1917.
[30] C.C. Hou, L. Zou, Q. Xu, A Hydrangea-like superstructure of open carbon cages with hierarchical porosity and highly active metal sites, Adv. Mater. 31 (2019) 1904689.
[31] J. Sun, H. Xue, Y.F. Zhang, X.L. Zhang, N. Guo, T. Song, H. Dong, Y. Kong, J. Zhang, Q. Wang, Unraveling the synergistic effect of Heteroatomic substitution and vacancy engineering in $CoFe_2O_4$ for superior Electrocatalysis performance, Nano Lett. 22 (2022) 3503–3511.
[32] H.F. Wang, C. Tang, B. Wang, B.Q. Li, Q. Zhang, Bifunctional transition metal Hydroxysulfides: room-temperature sulfurization and their applications in Zn–air batteries, Adv. Mater. 29 (2017) 1702327.
[33] X. Xu, M. Liu, Y. Nie, C. Wang, W. Wang, C. Liu, X. Wang, Z. Cai, X. Liu, S. Huo, B. Liu, J. Zou, Modulating electronic structure of interfacial Fe sites in Fe_2N/$CoFe_2O_4$ nano-heterostructure for enhancing corrosion-resistance and oxygen electrocatalysis in zinc-air battery, Chem. Eng. J. 471 (2023) 144639.
[34] J.J. Duan, R.L. Zhang, J.J. Feng, L. Zhang, Q.L. Zhang, A.J. Wang, Facile synthesis of nanoflower-like phosphorus-doped $Ni_3S_2/CoFe_2O_4$ arrays on nickel foam as a superior electrocatalyst for efficient oxygen evolution reaction, J. Colloid Interface Sci. 581 (2021) 774–782.
[35] H. Tong, X. Zheng, M. Qi, D. Li, J. Zhu, D. Jiang, Synergistically coupled CoMo/Fe_2O_3 electrocatalyst for highly efficient and stable overall water splitting, J. Colloid Interface Sci. 676 (2024) 837–846.
[36] Y.R. Liu, X. Shang, W.K. Gao, B. Dong, X. Li, X.H. Li, J.C. Zhao, Y.M. Chai, Y.Q. Liu, C.G. Liu, In situ sulfurized CoMoS/$CoMoO_4$ shell-core nanorods supported on N-

doped reduced graphene oxide (NRGO) as efficient electrocatalyst for hydrogen evolution reaction, J. Mater. Chem. A 5 (2017) 2885–2896.
[37] T. Wu, X. Ren, Y. Sun, S. Sun, G. Xian, G.G. Scherer, A.C. Fisher, D. Mandler, J. W. Ager, A. Grimaud, J. Wang, C. Shen, H. Yang, J. Gracia, H.J. Gao, Z.J. Xu, Spin pinning effect to reconstructed oxyhydroxide layer on ferromagnetic oxides for enhanced water oxidation, Nat. Commun. 12 (2021) 3634.
[38] M. Li, H. Li, H. Fan, Q. Liu, Z. Yan, A. Wang, B. Yang, E. Wang, Engineering interfacial sulfur migration in transition-metal sulfide enables low overpotential for durable hydrogen evolution in seawater, Nat. Commun. 15 (2024) 6154.
[39] Q. Zhao, Q. Zhang, Y. Xu, A. Han, H. He, H. Zheng, W. Zhang, H. Lei, U.-P. Apfel, R. Cao, Improving active site local proton transfer in porous organic polymers for boosted oxygen Electrocatalysis, Angew. Chem. Int. Ed. 63 (2024) e202414104.
[40] Y.F. Wu, J.W. Ma, Y.H. Huang, Enhancing oxygen reduction reaction of Pt–co/C nanocatalysts via synergetic effect between Pt and co prepared by one-pot synthesis, Rare Metals 42 (2023) 146–154.
[41] Z. Tan, L. Sharma, R. Kakkar, T. Meng, Y. Jiang, M. Cao, Arousing the reactive Fe sites in pyrite (FeS2) via integration of electronic structure reconfiguration and in situ electrochemical Topotactic transformation for highly efficient oxygen evolution reaction, Inorg. Chem. 58 (2019) 7615–7627.
[42] H. Zhang, A. Aierke, Y. Zhou, Z. Ni, L. Feng, A. Chen, T. Wågberg, G. Hu, A high-performance transition-metal phosphide electrocatalyst for converting solar energy into hydrogen at 19.6% STH efficiency, carbon, Energy 5 (2023) e217.
[43] X. Zheng, X. Han, Y. Cao, Y. Zhang, D. Nordlund, J. Wang, S. Chou, H. Liu, L. Li, C. Zhong, Y. Deng, W. Hu, Identifying dense $NiSe_2$/$CoSe_2$ Heterointerfaces coupled with surface high-valence bimetallic sites for synergistically enhanced oxygen Electrocatalysis, Adv. Mater. 32 (2020) 2000607.
[44] X. Peng, M. Zhang, H. Qin, J. Han, Y. Xu, W. Li, X. Zhang, W. Zhang, U. Apfel, R. Cao, Switching Electrocatalytic hydrogen evolution pathways through electronic tuning of copper porphyrins, Angew. Chem. Int. Ed. 136 (2024) e202401074.
[45] J. Mou, Y. Li, L. Ou, J. Huang, A highly-efficient electrocatalyst for room temperature sodium-sulfur batteries: assembled nitrogen-doped hollow porous carbon spheres decorated with ultrafine α-MoC_{1-x} nanoparticles, Energy Storage Mater. 52 (2022) 111–119.
[46] Y. Han, L. Zhao, W. Cheng, M. Wang, L. Yang, Y. Lin, K. Xu, Iridium cluster anchored onto cubic molybdenum carbide with strong electronic interactions for robust hydrogen oxidation reaction in alkaline medium, Adv. Funct. Mater. 34 (2024) 2407060.
[47] X. Liu, K. Deng, P. Liu, X. Lv, W. Tian, K. Ma, H. Li, J. Ji, Mutual promotion by structural design and intrinsic activity coupling of CNTs/MoC/CoNiMo for water splitting and urea electrolysis, Appl. Catal. B Environ. 343 (2024) 123470.
[48] Y.G. Ji, J. Wu, H. Wen, S. Wang, L. Feng, Step-by-step enhancing oxygen evolution ability of $CoFe_2O_4$ by hybrid structure engineering and fluorine doping, Chem. Eng. J. 496 (2024) 154211.
[49] T. Chao, W. Xie, Y. Hu, G. Yu, T. Zhao, C. Chen, Z. Zhang, X. Hong, H. Jin, D. Wang, W. Chen, X. Li, P. Hu, Y. Li, Reversible hydrogen spillover at the atomic interface for efficient alkaline hydrogen evolution, Energy Environ. Sci. 17 (2024) 1397–1406.
[50] Z. Liang, G. Zhou, H. Tan, Y. Mou, J. Zhang, H. Guo, S. Yang, H. Lei, H. Zheng, W. Zhang, H. Lin, R. Cao, Constructing $Co_4(SO_4)_4$ Clusters within Metal–Organic Frameworks for Efficient Oxygen Electrocatalysis, Adv. Mater. 36 (2024) 2408094.
[51] Q. Zhang, W. Zhang, J. Zhu, X. Zhou, G.R. Xu, D. Chen, Z. Wu, L. Wang, Tuning d–p orbital hybridization of $NiMoO_4$@$Mo_{15}Se_{19}$/$NiSe_2$ Core-Shell nanomaterials via asymmetric coordination interaction enables the water oxidation process, Adv. Energy Mater. 14 (2024) 2304546.